NiCuAg: An Electrochemically-Synthesised Trimetallic Stack for CO_2 Reduction

Hannah L.A. Dickinson , Mark D. Symes

PII: S0013-4686(24)00597-8
DOI: https://doi.org/10.1016/j.electacta.2024.144355
Reference: EA 144355

To appear in: *Electrochimica Acta*

Received date: 7 February 2024
Revised date: 25 April 2024
Accepted date: 27 April 2024

Please cite this article as: Hannah L.A. Dickinson , Mark D. Symes , NiCuAg: An Electrochemically-Synthesised Trimetallic Stack for CO_2 Reduction, *Electrochimica Acta* (2024), doi: https://doi.org/10.1016/j.electacta.2024.144355

NiCuAg: An Electrochemically-Synthesised Trimetallic Stack for CO_2 Reduction

Hannah L.A. Dickinson and Mark D. Symes*

WestCHEM, School of Chemistry, University of Glasgow, Glasgow, G12 8QQ, United Kingdom

** Email: mark.symes@glasgow.ac.uk*

Abstract

Electrochemical CO_2 reduction is a promising technique for the production of desirable hydrocarbons without the need to resort to fossil resources. However, high overpotentials and poor selectivity remain a challenge for CO_2 electro-reduction, especially for deep reduction by more than two electrons. One apparently attractive approach for breaking the scaling relations caused by simultaneous CO_2 reduction pathways and for achieving deeper reduction is the use of multi-metallic electrodes, where several promising metal catalysts are present in close proximity. Herein, noting the activity shown by Ni, Cu and Ag for CO_2 electroreduction when used individually, we set out to synthesise a tri-metallic "stack" catalyst, NiCuAg, and then to test this for electrochemical CO_2 reduction. The stack architecture was successfully generated and the trimetallic NiCuAg system did show improved Faradaic efficiency for the reduction of CO_2 to formic acid when compared to the bare Ni and bimetallic NiCu controls under some select conditions. However, the two-layer NiCu stack and bare Ni exhibited consistently higher Faradaic efficiencies than NiCuAg for deeper CO_2 electroreduction to methanol and ethanol, indicating that the combination of three individually

promising metals does not necessarily translate into superior catalytic performance for deep carbon dioxide reduction.

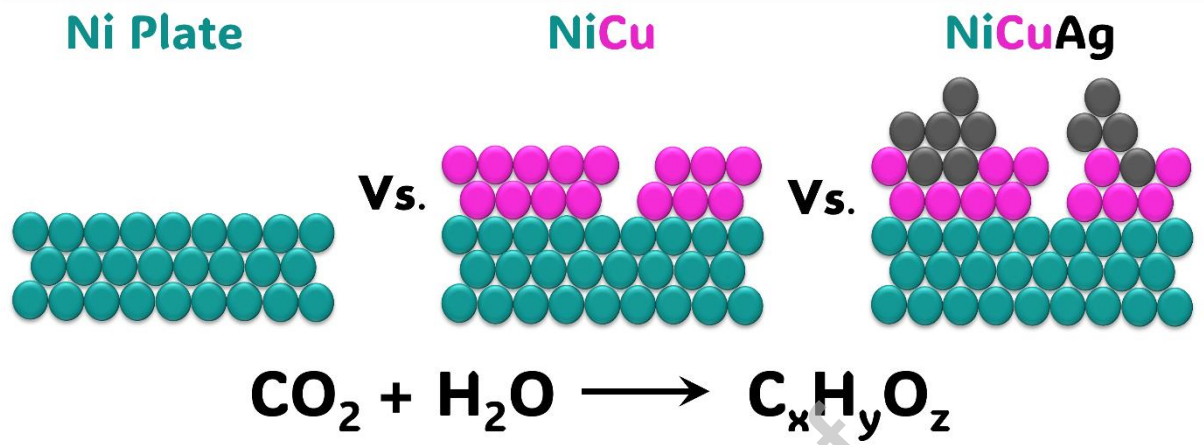

Keywords: carbon dioxide reduction; electrocatalysis; copper alloys; tandem catalysis; multi-metallic catalyst

1. Introduction

Increased levels of carbon dioxide in the atmosphere compared to before the industrial revolution have led to intensified research into more sustainable energy and feedstock sources, to prevent further increases in emitted CO_2.[1–3] This atmospheric CO_2 can provide a useful feedstock for the storage of excess renewably-generated energy.[4–7] The electroreduction of CO_2, powered by renewables, has been suggested as a means of closing the carbon gap[8] whilst producing desirable, economically viable chemical feedstocks.[9] At least sixteen carbon products, including carbon monoxide, formic acid, methane, ethylene, and ethanol are commonly formed by electrochemical CO_2 reduction;[10] however, since the reaction is typically performed under aqueous and ambient conditions, hydrogen evolution is always a competing process.[11,12] This wide product range and competitive hydrogen evolution leads to poor selectivity and low energy efficiency.

Metal electrocatalysts have been a significant focus since Hori's seminal discovery that Cu can reduce CO_2 by more than two electrons to produce hydrocarbons.[13] Since CO_2 reduction proceeds via

many simultaneous pathways[14,15] (wherein the reaction intermediates are approximately linearly related),[16] these scaling relations must be broken to achieve a high selectivity for a given product at a low overpotential. Thus, methods such as tethering, ligand stabilisation, mixed metal phases and alloying have been employed.[17] These are beneficial methods for directing morphology and composition and, accordingly, geometric and electronic environments.[18] Bimetallic catalysts, particularly those containing Cu, have garnered significant interest as they potentially allow two different metal sites to be in close proximity to a single reacting absorbate;[18–25] conversely, reported examples of trimetallic electrocatalysts for CO_2 reduction are much rarer. The interaction of these neighbouring active sites has been suggested to create what is termed a synergistic effect, whereby the activity of the combination of metals is mutually reinforced and thus greater than the sum of the activities of the separate components.[26] The term synergistic effect appears to have first been used in relation to CO_2 reduction by Watanabe et al.[27] upon the discovery that Cu-Ni alloys produced methanol as a CO_2 reduction product whilst the individual metals did not. Despite the development of electroreduction and detection systems that have disproven the effect in this case, the term is still employed.[20] Apparent synergies can often be explained by one of the following influences:[20,28] (a) the promotion of desorption by dipole repulsion from the secondary metal,[29] (b) a bifunctional mechanism[30–32] whereby the secondary metal can stabilise an intermediate for reaction at the primary metal, and (c) spillover[33–35] wherein the close proximity of the metal active sites allows an excess of one intermediate to be produced (for example CO), leading to an increase in local concentration of that intermediate for further reduction on the other metal active sites.

In 2022 Zhu et al.[34] developed a AuAgCu heterostructure using a multi-step seed-mediated growth method to form a Au core encapsulated by Ag. Cu was selectively deposited on one side of the nanorod to give an asymmetric nanostructure. CO_2 reduction tests resulted in a Faradaic efficiency towards ethanol of 38% at −0.8 V vs. reversible hydrogen electrode (RHE). This enhanced activity was attributed to the promotion of C-C coupling at Cu sites. The catalysts' asymmetric design

allowed for a CO spill-over process to occur, whereby weakly-bound CO was released from the Au and Ag sites, increasing the local concentration at the Cu sites to allow for C-C coupling.

Chaitree et al.[36] synthesised a Cu-Ni-Sn electrocatalyst on Pd-activated carbon fabric by electroless deposition. Testing in an H-cell showed decreased activity towards H_2 production compared to the other bi/monometallic catalysts that were tested; whilst a Faradaic efficiency of 12% towards acetone was claimed at −1.6 V vs. Ag/AgCl. The total Faradaic efficiency for C_{2+} products, including ethylene glycol, acetate, ethanol, 1-butanol, and acetone, was 37%.

Zhang et al.[37] assembled a Cu-Zn-Al layered double hydroxide electrocatalyst. CuZn alloys and CuZn aluminate oxides were stacked in alternating layers. The intention was to create many active sites by generating strong electronic interactions between the three metals in different oxidation states. The layered system achieved a Faradaic efficiency of 89% towards C_{2+} products in a flow-cell reactor at −1.15 V vs. RHE. This included Faradaic efficiencies of over 30% respectively for both ethylene and ethanol.

Herein we report an electrochemically synthesised trimetallic stack for CO_2 reduction, NiCuAg. We define “stack” here as being sequentially-coated metal layers. A multi-metal layered design was chosen to attempt to break the typical linear scaling relations seen in single metal CO_2 electroreduction catalysts. Previous studies have shown the combination of Cu and Ni to be promising. Zhang et al. achieved a Faradaic efficiency of 62% for C_{2+} products at −0.88 V vs. RHE with a Ni-Cu nanowire catalyst.[38] Similarly, Suzuki et al. developed a Cu-Ni nanoparticle catalyst that achieved a 35% Faradaic efficiency for C_2 products at −1.2 V vs. RHE.[39] Ag was added to our catalyst as a final layer inspired by Choi et al., where it was found that the addition of Ag promoted CO binding on Cu sites, allowing reduction to methane at a 72% Faradaic efficiency at −1.17 V vs. RHE.[40]

It is generally accepted that single metals fall into several groups when used for the electrochemical reduction of CO_2.[41,42] Metals with a high H affinity (Fe, Ni, Pd, Pt) primarily produce hydrogen and are not active towards CO_2 reduction. Metals which coordinate CO strongly to produce CO (Ag, Au, Zn)

form another group, and those which produce formic acid (Cd, In, Sn) are another. Cu, which has moderate (intermediate-strength) binding and thus can produce methane as well as products that require C-C coupling, is often given its own category.[42] Ni, Cu and Ag were chosen for our catalyst based on these groupings: Ni, for its high H affinity and good proton transfer ability; Cu, for its C-C coupling and further reduction ability; and Ag for its CO coordination ability. Despite the fact that Ni is typically associated with increased hydrogen evolution activity,[43,44] it has been shown that nickel based catalysts have the ability to promote C-C coupling.[45] Indeed a Ni-Al catalyst was one of the first Cu-free electrocatalysts to be shown to produce C_2 and C_3 products by CO_2 reduction.[46] More generally, it has been suggested that the combination of additional metals with Ni would help to overcome the non-desirable features of pure Ni metal, such as CO poisoning and nanoparticle sintering.[45,47]

Our hypothesis was therefore that a synergistic effect and improved selectivity for C_{2+} products would be observed at lower potentials by combining the metals Cu, Ni and Ag. This hypothesis was based on the idea that CO_2 would firstly be reduced to CO on the Ag metal through well-studied mechanisms[48–51], and would then spill over onto Cu sites for further reduction to C_{2+} products. The Ni was incorporated both for its own C-C bond forming ability, and also for its high affinity for H atoms, which we postulated might facilitate the hydrogenation of the C_{2+} products formed on the adjacent copper sites to give highly-reduced multi-carbon products.

We used a sequential synthesis approach to produce active sites in which all three metals would be present at the surface and exposed to the electrolyte.[39,40] However, our results suggest that there is no evidence for significant beneficial synergism by combination of these metals, with a bimetallic mixture of Ni and Cu displaying similar activity for methanol and ethanol production to an Ni cathode, and both of these displaying significantly better performance than the trimetallic NiCuAg material. Clearly then, not every combination of promising metals leads to improved selectivity for deep CO_2 electroreduction activity.

2. Experimental

2.1 Materials

Nickel foil (0.5 mm, [7440-02-0], annealed, 99.5 %), copper (II) sulfate ([7758-98-7], anhydrous, 98%), and potassium hydrogen carbonate ([298-14-6], 99%) were obtained from Alfa Aesar. Silver nitrate ([7761-88-8], ACS reagent, >99%) was obtained from Sigma Aldrich. Nafion-117 membranes were obtained from Fuel Cell Store. Carbon Dioxide (99.8%, Industrial Grade) and Argon (99.9%) were supplied by BOC Limited. All chemicals were used as received without further purification and all solutions were produced using ultrapure water (15.8 MΩ-cm).

2.2 Catalyst Preparation

Nickel foil was cut to a size of 2 × 1 cm and the backside covered using Sellotape. This was used as the working electrode. The Ni surface was cleaned prior to any coating by sonication for 10 minutes each in: acetone, followed by isopropyl alcohol and finally deionised water. Copper electrodeposition (from a solution of 0.1 M $CuSO_4$ at −200 mV vs. Ag/AgCl) was completed in an open beaker for 10 minutes whilst stirring. For copper deposition, a standard three-electrode setup was used: leak-free Ag/AgCl reference electrode (Innovative Instruments, Inc.), Ni foil working electrode, and graphite rod (Alfa Aesar) counter electrode. Where appropriate, a silver layer was added by galvanic replacement by placing the NiCu stack in a 0.01 M $AgNO_3$ solution for two minutes, without stirring, to give NiCuAg. All catalysts were prepared at room temperature and pressure.

2.3 Characterisation

The surface morphology of the prepared electrocatalyst plates was analysed in the Geoanalytical Electron Microscopy and Spectroscopy (GEMS) facility at the School of Geographical and Earth Sciences, University of Glasgow, using a Carl Zeiss Sigma variable pressure analytical Scanning

Electron Microscope (SEM) with Oxford Microanalysis with a 15 kV accelerating voltage. A 20 nm thick carbon layer was coated onto the samples prior to analysis. Cross-sectional Transmission Electron Microscopy (TEM) was completed at the Kelvin Nanocharacterisation Centre. A cross-sectional TEM lamella was extracted from the bulk sample and transferred onto a Cu TEM grid using a FEI Nova NanoLab 200 dual beam SEMFIB. The TEM imaging and analysis was done on a JEOL Atomic Resolution Microscope (JEM-ARM200cF) STEM, operating at 200 kV. This microscope is equipped with a cold field emission gun and a CEOS (Corrected Electron Optical Systems GmbH) probe corrector for STEM imaging and a Gatan GIF Quantum electron spectrometer for electron energy-loss spectroscopy (EELS).

X-ray diffraction (XRD) was undertaken using a Rigaku MiniFlex benchtop diffractometer equipped with Cu sealed tube X-ray source. The surface composition of the catalysts was analysed by X-ray photoelectron spectroscopy (XPS) at the University of St Andrews using a Scienta 300 with a SPECS monochromated X-Ray source. All data analyses and fittings were made using CasaXPS software.

2.4 Electrochemical Characterisation

Electrochemical studies were controlled by a Gamry interface 1010E potentiostat, at room temperature and pressure. Linear sweep voltammograms and electrochemical CO_2 reduction experiments were carried out in a custom-made air-tight two-compartment H-cell (Figure 1) under a constant flow of Ar or CO_2. A graphite rod and leak-free Ag/AgCl electrode were used as the counter and reference electrodes respectively. A Nafion-117 membrane was added to separate the anolyte and catholyte, alongside preventing the diffusion and re-oxidation of any reduction products. 0.1 M $KHCO_3$ was used as the electrolyte; it was purged with CO_2 or Ar gas for at least 30 minutes prior to testing. Linear sweep measurements were taken between +0.2 and −2.0 V vs. Ag/AgCl with a scan rate of 25 mV/s.

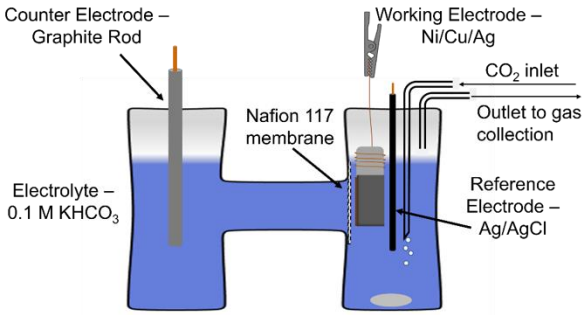

Figure 1. Custom air-tight H-cell set-up, as used for electrochemical CO_2 reduction tests.

2.5 Product Analysis

2.5.1 Gas Product Analysis

Possible gas products (H_2, CO, CH_4, C_2H_6 and C_2H_4) were flushed from the cell by the constant stream of Ar or CO_2 and collected in a gas sampling bag, and analysed post-electrolysis by gas chromatography (Agilent 8860) equipped with 2 Porapak Q columns and a MoleSieve 13X column. A thermal conductivity detector was used. Gas products were tested after CO_2 reduction experiments were completed. A gas chromatogram showing all possible peaks and the standard calibration curves are shown in Supplementary Figures S1 and S2.

2.5.2 Liquid Product Analysis

Liquid phase products were quantified by 1D ^{1}H Nuclear Magnetic Resonance (NMR) spectroscopy (400 MHz, Bruker). 400 μL of the post-electrolysis electrolyte solution was mixed with 70 μL D_2O ([7789-20-0], 99.9% D, Goss Scientific) and 30 μL of internal standard solution for analysis. The internal standard consisted of 10 mM dimethyl sulfoxide-D6 ([67-68-5], 99.9% D, Cambridge Isotope Laboratories, Inc) and 50 mM phenol ([108-95-2] ⩾99.0%, Sigma Aldrich) prepared in 100 mL 0.1 M $KHCO_3$. The water suppression method was used to record the ^{1}H spectra. The relative peak area was compared to the first phenol peak (7.32 ppm); the ratio of the area of a given peak was compared with the standard curve to quantify the concentration produced. A typical sample ^{1}H NMR

spectrum and the standard calibration curves are shown in Supplementary Figures S3 and S4 and Table S1.

2.5.3 Faradaic Efficiency Calculations

Faradaic efficiency expresses the selectivity for a particular product from an electrochemical reaction; it is calculated using Equation 1, where a is the number of transferred electrons according to the relevant balanced chemical equation, n is the number of moles of a given product, F is Faraday's constant, and Q_{total} is the total charge passed.

$$\text{Faradaic Efficiency} = \frac{a \times n \times F}{Q_{total}} \times 100 \quad (1)$$

3. Results and discussion

3.1 Catalyst Preparation and Characterization

We first synthesised a NiCu stack by electrodeposition of copper. The deposition potential of copper was found by taking a cyclic voltammogram of $CuSO_4$ (Figure 2a). A reduction peak at -0.16 $V_{Ag/AgCl}$ and an oxidation peak at 0.15 $V_{Ag/AgCl}$ were seen. Thus, electrodeposition was carried out at -0.2 $V_{Ag/AgCl}$ for 600 seconds; a shiny red/brown Cu layer was seen on the Ni surface (Figure 2b and 2d). A silver layer was then added by galvanic replacement (Figure 2c and 2e); Cu acts as a sacrificial template, it is oxidised by Ag^+ due to the favourable difference in reduction potentials between copper and silver, 0.80 V Ag^+/Ag compared to 0.34 V for Cu^{2+}/Cu. Thus, some of the Cu layer is spontaneously replaced by Ag, upon submersion of the NiCu plate in a $AgNO_3$ solution for 2 minutes. This immersion period was selected as it is insufficient for complete replacement of the Cu by Ag (see Figures 3 and 4 for example).

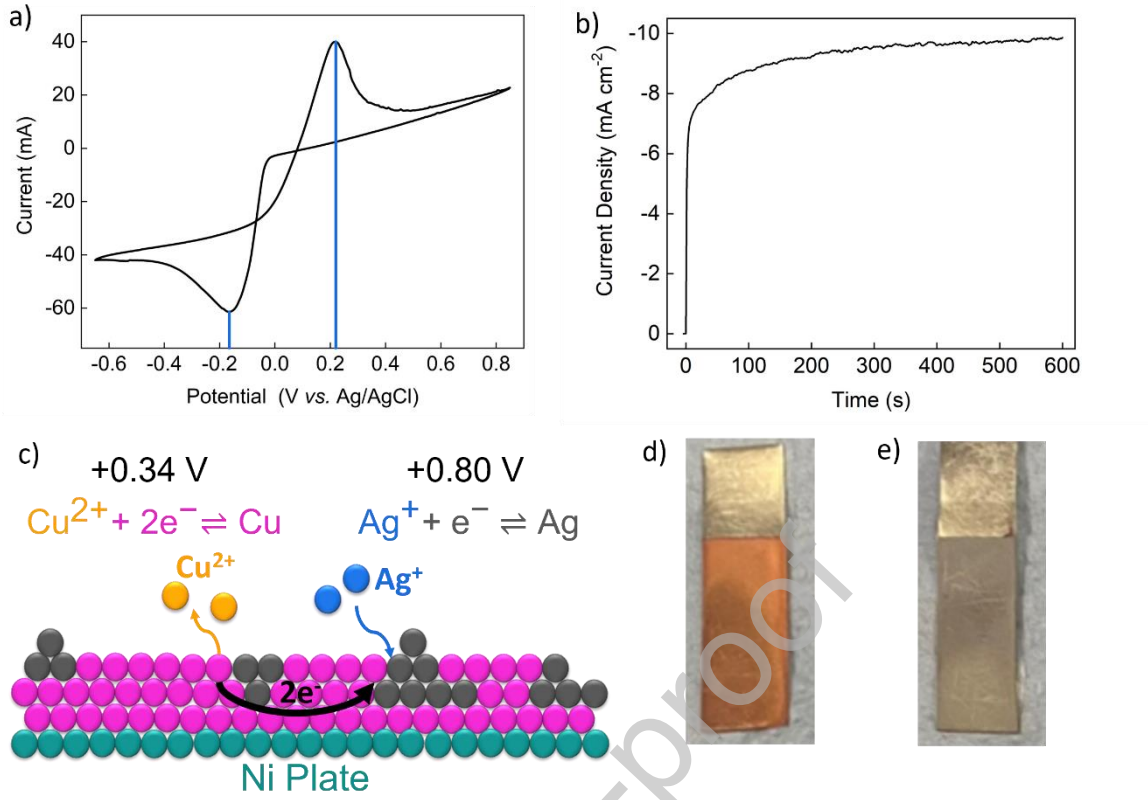

Figure 2. a) Cyclic voltammogram of 0.1 M $CuSO_4$ in a three-electrode set-up (Ni plate as the working electrode, leak-free Ag/AgCl as the reference electrode, and graphite rod as the counter electrode), at a scan rate of 25 mV s^{-1}; blue drop lines represent the reduction (−0.16 $V_{Ag/AgCl}$) and oxidation (0.15 $V_{Ag/AgCl}$) peaks. b) Bulk electrolysis to coat a Cu layer on Ni at −0.2 $V_{Ag/AgCl}$. c) Schematic of the galvanic replacement of Cu by Ag. d) Photo of an as-synthesised NiCu electrode. e) Photo of an as-synthesised NiCuAg electrode.

Following their synthesis, the NiCu and NiCuAg films, and also a bare Ni plate were characterised by X-ray diffraction (XRD), scanning electron microscopy (SEM) with elemental mapping, and X-ray photoelectron spectroscopy (XPS). The NiCu and NiCuAg electrodes were also analysed by cross-sectional transmission electron spectroscopy (TEM) followed by electron energy-loss spectroscopy (EELS).

SEM and elemental mapping were employed to investigate the surface of the catalysts. SEM

images of NiCu and NiCuAg are shown in Figure 3. Bulbous florets of Cu nanoparticles can be seen on the Ni surface for both catalysts. A groove in the Ni surface can be seen in the NiCu images (Figure 3a & 3b): this is an outcome of the Ni plate manufacturing process, and as a result essentially no Cu is coated in that area. Figure 3e & 3f clearly show dendritic Ag particles that reach across the NiCuAg surface. Elemental mapping by energy dispersive X-ray spectroscopy confirms the identity of each metal and shows that they are distinctly stacked on top of one another in layers. Yet, there are areas where Ni, and Cu are both exposed as well as the Ag. Thus, CO_2 (or its intermediate reduction products) should be able to bind on all the metal sites and benefit from the binding abilities of all three metals for various intermediates.

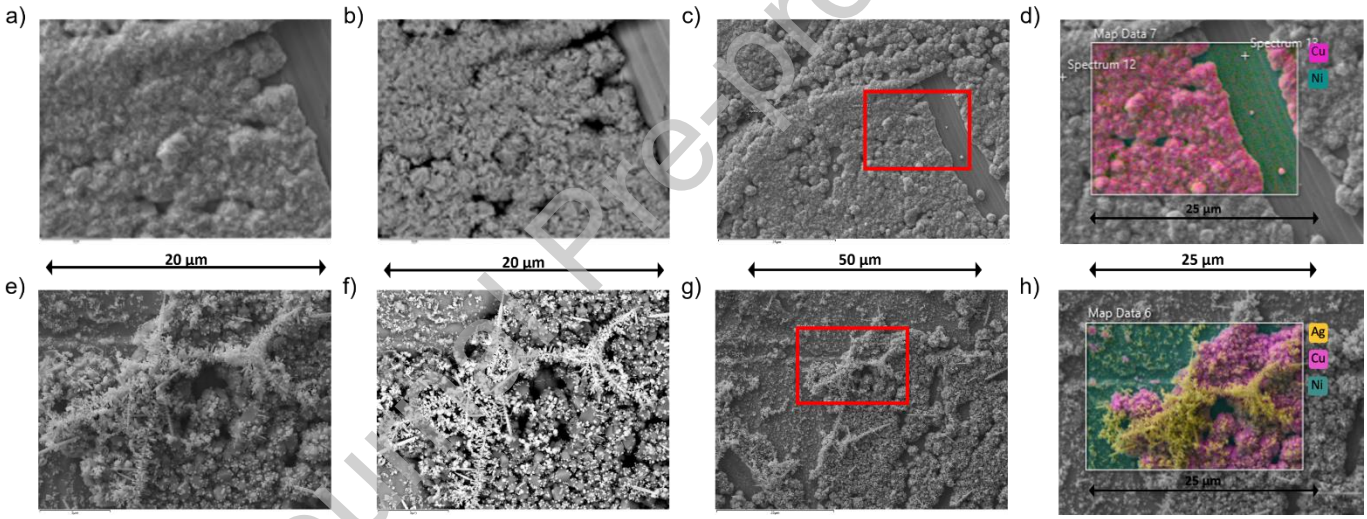

Figure 3. a) SEM image of NiCu. b) Backscattered electron image of NiCu. c) NiCu elemental mapping area. d) NiCu energy-dispersive X-ray spectroscopy (EDX) elemental map. e) SEM image of NiCuAg. f) Backscattered electron image of NiCuAg. g) NiCuAg elemental mapping area. h) NiCuAg EDX elemental map. For both electrode elemental maps: teal corresponds to Ni, pink to Cu and yellow to Ag.

Figure 4 shows the cross-sectional TEM lamellae of the NiCu and NiCuAg electrodes. Figure 4a clearly shows the nickel and copper layers of the NiCu electrode. Both layers are polycrystalline, with Cu showing smaller grains than Ni. The deposited Cu layer was calculated to be between 1 and 1.5

µm thick. The boundary between the Ni and Cu layer is roughly outlined by the black dashed line. The boundary between the electrodeposited Cu and the Pt, deposited as part of the imaging process, is illustrated by a blue dashed line. Both boundaries are confirmed by electron energy-loss spectroscopy (EELS) – see further details in the Supplementary Information (Figures S5 and S6). For the NiCuAg plate, high-angle annular dark-field STEM imaging was used to create a suitable contrast between layers (Figure 4b). The Ni and Cu layers are clearly defined with the boundary depicted by a dashed line. The bright areas visible on the Cu surface are due to Ag. This further confirms the uneven distribution of Ag seen in the SEM images above. Figure 4b suggests that in some areas the Ag thickness could be up to 1 µm whilst at other points there is no Ag present. It can also be seen that the galvanic replacement of Ag produces an irregular surface, increasing the surface area for reductions to occur. Elemental analysis/EELS of the NiCuAg plate can be found in the Supplementary Information (Figures S7 and S8).

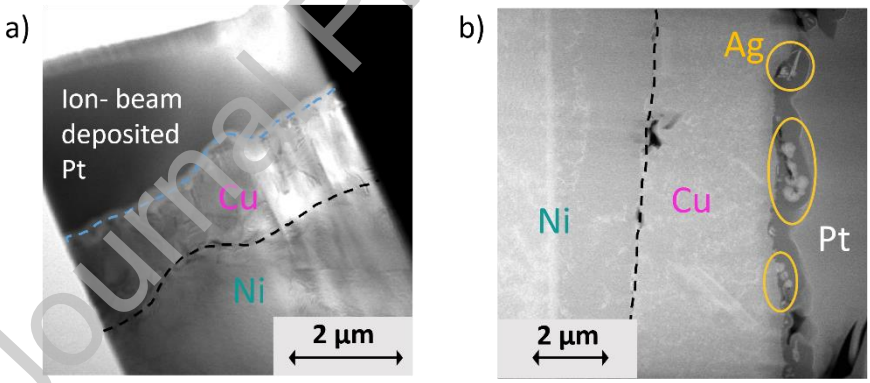

Figure 4. a) Bright field STEM image of the fabricated NiCu lamella. b) High-angle annular dark-field (HAADF) STEM image of the fabricated NiCuAg lamella. In both cases, the black dashed lines indicate the Ni/Cu boundary. The blue dashed line in panel a) indicates the Cu/Pt boundary. This is more difficult to pinpoint on the NiCuAg sample, but Ag can be seen (ringed in orange).

Figure 5 compares the XRD patterns of the Ni plate and as-synthesised NiCu and NiCuAg; only peaks related to the corresponding metals as defined by the PDF cards (Ni PDF no. 9009862, Cu PDF no.

4105040 and Ag PDF no. 9013047) and NiO (PDF no. 9008693) are observed. For Ni, the key peaks occur at 44.6°, 52.0° and 76.6°, which can clearly be seen in the spectrum. Standard Cu peaks appear at 43.7°, 51.0° and 74.9°. These peaks are present in the NiCu sample at low intensity, which is consistent with the difference in layer thickness between the Cu layer and the Ni plate. For the NiCuAg sample the Cu peaks present in the NiCu sample are diminished and new peaks corresponding to the new top layer of Ag are present. The peaks at 37.8°, 44.0° and 76.7° correspond to this added Ag layer. Although the peaks of pure Ni, Cu and Ag are in similar positions, it is clear from the XRD that the additional layers have been coated and no major impurity peaks are present, save for some NiO.

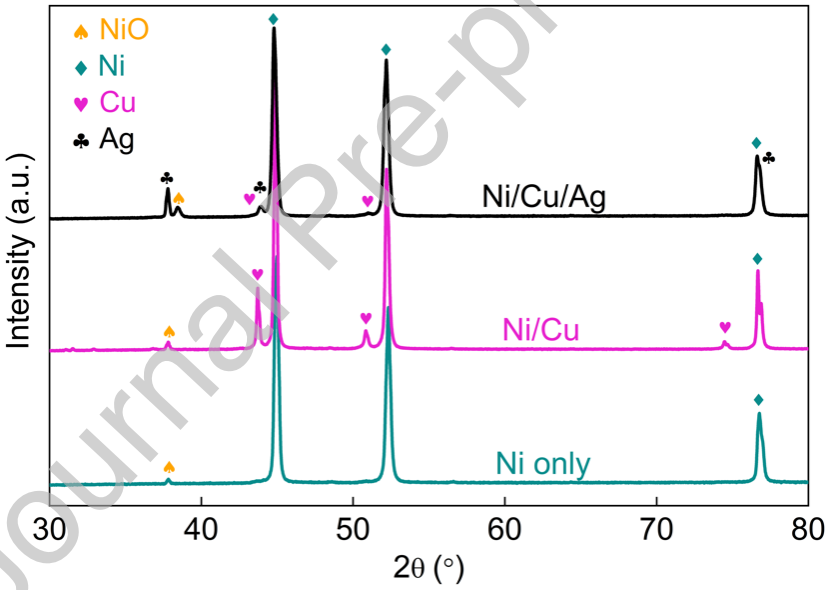

Figure 5. Stacked XRD patterns for Ni, NiCu and NiCuAg. Teal diamonds signify peaks relating to Ni (PDF no. 9009862), orange spades signify NiO peaks (PDF no. 9008693), pink hearts represent Cu peaks (PDF no. 4105040), and black clubs signify Ag peaks (PDF no. 9013047).

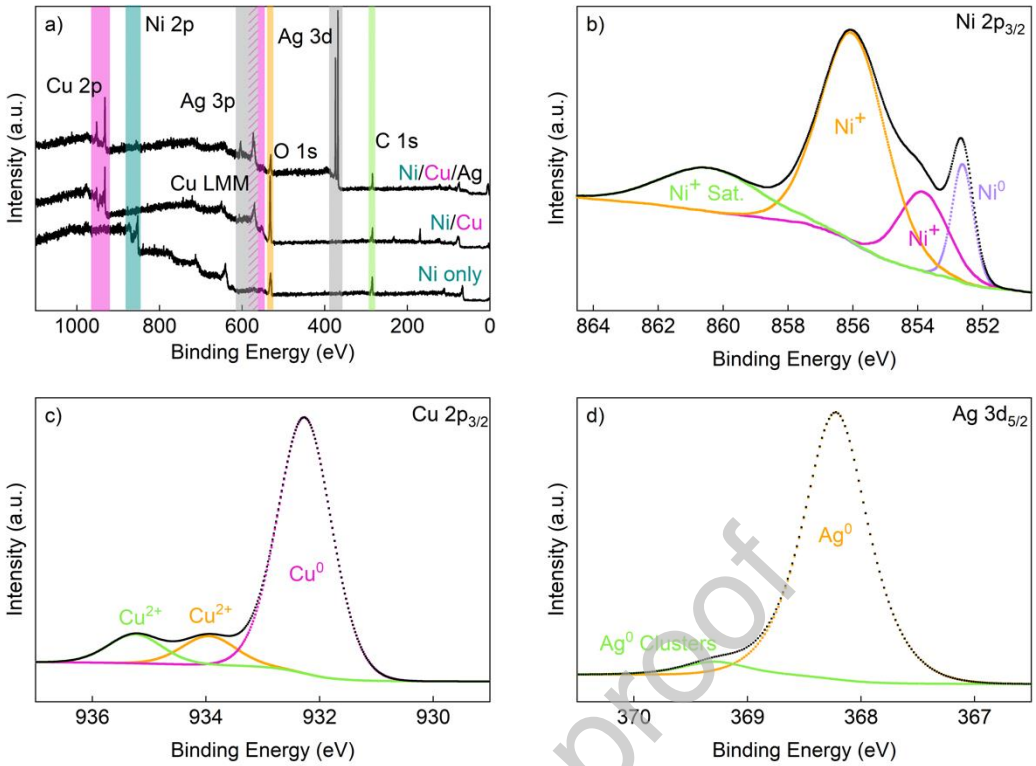

Figure 6. X-ray photoelectron spectroscopy survey spectra of a) each stage of the synthesised catalyst stack. Deconvoluted high resolution XPS spectrum of the NiCuAg stack: b) Ni $2p_{3/2}$; c) Cu $2p_{3/2}$; d) Ag $3d_{5/2}$. Data analysis and fittings were performed in CasaXPS software. Peak assignments were made using the NIST X-ray Photoelectron Spectroscopy Database,[52] and Perkin-Elmer Handbook of X-ray Photoelectron Spectroscopy.[53]

The chemical states and surface electronic structure of the catalyst plates at each stage of synthesis were investigated by X-ray photoelectron spectroscopy. This allowed the identification of surface oxides which are present in low quantities and whose presence is hard to detect by bulk techniques like XRD. Figure 6a shows that a survey spectrum of the bare Ni plate evinces the presence of C (285 eV, C 1s), O (531 eV, O 1s), and Ni (855 eV, Ni 2p). The NiCu spectrum shows additional peaks resulting from Cu (934 eV for Cu 2p and 590 eV for Cu LMM) and the addition of the Ag layer gives further peaks (610-590 eV for Ag 3p and 369 eV for Ag 3d) in the NiCuAg spectrum. Upon coating with Cu, and further Ag, the Ni signal at 855 eV is significantly decreased. This suggests that the Cu coating is sufficiently thick that the Ni plate below is no longer detected (at least on the areas

analysed). However, the final Ag layer is sufficiently discontinuous for the underlying Cu to still be detectable by XPS.

From the NiCuAg catalyst survey scan, the binding energy difference between Cu $2p_{1/2}$ and Cu $2p_{3/2}$ was 19.9 eV: this is typical of metallic Cu with an oxidised layer containing $CuO/Cu(OH)_2$ on the surface.[54] The binding energy difference between the Ag $3d_{3/2}$ and Ag $3d_{5/2}$ was 6.0 eV, characteristic of metallic Ag.[53]

The deconvoluted high-resolution spectra for each of the metals within the NiCuAg stack (Fig. 5b-5d), reveal further detail about the coated species. Binding energies and peak assignments are given in Table 1. The Ni spectrum, focused on the Ni $2p_{3/2}$ region, shows the presence of multiple Ni-containing species. The largest peak, at 856.0 eV, is attributed to NiO, whilst the peak at 852.6 eV is assigned to metallic Ni. Since measures to a depth of approximately 5 nm and there are coated layers above the Ni plate, surface NiO is preferentially seen in the Ni XPS spectrum, Fig 6c. However, when the bare Ni plate is analysed (Fig. S10) the peak assigned to metallic Ni appears to be more pronounced and the adsorbed surface NiO makes less of a contribution. This further confirms the presence of oxygen at the interface between the metals as seen by TEM. The high-resolution Cu spectrum shows the Cu $2p_{3/2}$ region. The three peaks reveal that the Cu layer consists mostly of metallic Cu species with some Cu^{2+} oxides. These have been assigned as CuO and $Cu(OH)_2$; these Cu oxides may have formed during electrodeposition[55–58] or via oxidation of the coated metallic Cu during drying. The Ag $3d_{5/2}$ spectrum is deconvoluted to reveal two peaks, the largest at 368.2 eV is attributed to metallic silver. The secondary peak at 369.3 eV results from the agglomeration of Ag particles to form clusters on the surface.[59] Thus, although there are no oxide species in the top Ag layer, both the Cu and Ni layers of the catalyst displayed peaks characteristic of their oxides. High resolution spectra for the NiCu and Ni catalyst plates, and the corresponding binding energies and peak assignments can be found in the Supplementary Information (Figures S9 and S10, and Tables S2 and S3).

Table 1: XPS binding energies for the NiCuAg catalyst stack. Binding energies calculated relative to C 1s = 285.0 eV.

Element	*Binding energy/ eV*	*Assignment*	*References*
Ni $2p_{3/2}$	852.6	Ni^0	60
	853.8	Ni^+ - NiO_{ads}	61
	856.0	Ni^+ - NiO	62
	860.4	Ni^+ - satellites	60
Cu $2p_{3/2}$	932.2	Cu^0	63
	933.9	Cu^{2+} - CuO	64
	935.3	Cu^{2+} - $Cu(OH)_2$	65
Ag $3d_{5/2}$	368.2	Ag^0	66,67
	369.3	Ag^0 clusters	59

3.2 Electrochemical tests

3.2.1 Linear Sweep Voltammetry

Linear sweep voltammetry was undertaken to measure and compare the activities of the bare Ni plate, NiCu, and NiCuAg in CO_2-saturated $KHCO_3$ and Ar-saturated $KHCO_3$, across a range of potentials (Figure 7). Little to no current flow was seen in both the CO_2-purged electrolyte (solid lines) or the argon-purged electrolyte (dashed lines) until a potential of around −0.4 V_{RHE} was reached, at which point appreciable current began to flow. Since this happens regardless of whether CO_2 is present or not, this current can be attributed to the onset of the background hydrogen evolution reaction.

In the Cu-containing materials, a shoulder manifests at around −0.5 V_{RHE} in argon; this feature is well documented.[13,15,68] This has been ascribed to the reduction of CO or related species (manifesting from the carbonate electrolyte) adsorbed on the surface of the electrode.[68,69] In support of this assertion, this shoulder becomes more pronounced in the presence of CO_2 (e.g. black solid line), suggesting that this wave is indeed due to reduction of CO or related species. In order to determine

the products of any CO_2 reduction occurring via the process underlying this wave, we conducted bulk electrolysis across a range of potentials, starting from −0.29 V_{RHE}.

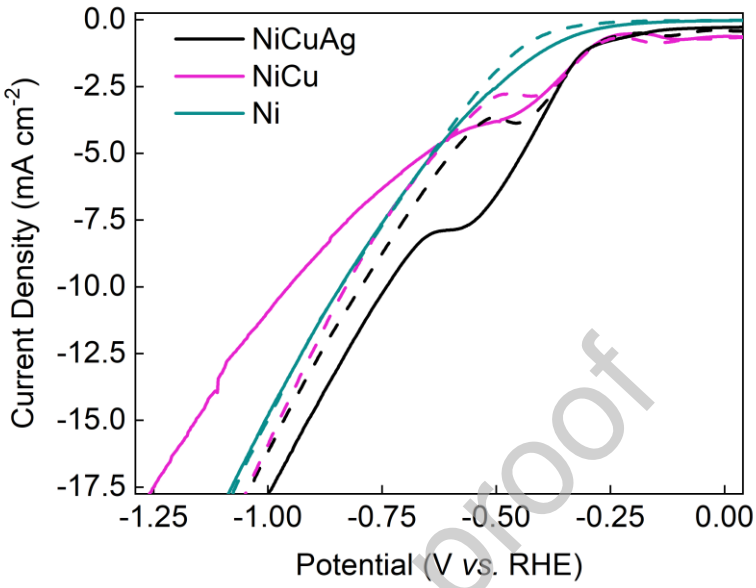

Figure 7. Linear Sweep Voltammetry at a sweep rate of 25 mV s^{-1}, of pure Ni (teal), NiCu (pink) and NiCuAg (black) in CO_2-saturated 0.1 M $KHCO_3$ (solid lines) and Ar-saturated 0.1 M $KHCO_3$ (dashed lines).

3.2.2 Bulk electrolysis

The electrochemical CO_2 reduction activity and selectivity of the catalyst stacks and bare Ni plate were tested in a custom air-tight H-cell (Figure 1). CO_2-saturated 0.1 M $KHCO_3$ solution (pH = 6.8) was used as the electrolyte. Testing was performed at fixed potentials between −0.29 V_{RHE} and −1.09 V_{RHE} at 0.20 V intervals. CO_2 was continually flowed through the set-up to flush the gas products into the gas collection bag; therefore, experiments were carried out until the attached gas collection bag had reached its capacity (2 L). Consequently, experiment length ranged but typically lasted around 40 minutes.

Figure 8a shows bulk electrolysis using the NiCuAg catalyst at a variety of potentials. At all potentials tested, there is a decrease in current density at the experiment outset. After this initial decrease, the current density appears to become more stable; however, in all cases it continues to decrease,

though at a slower rate. The average current density measured over the electrolysis for each potential can be found in the Supplementary Information (Table S4).

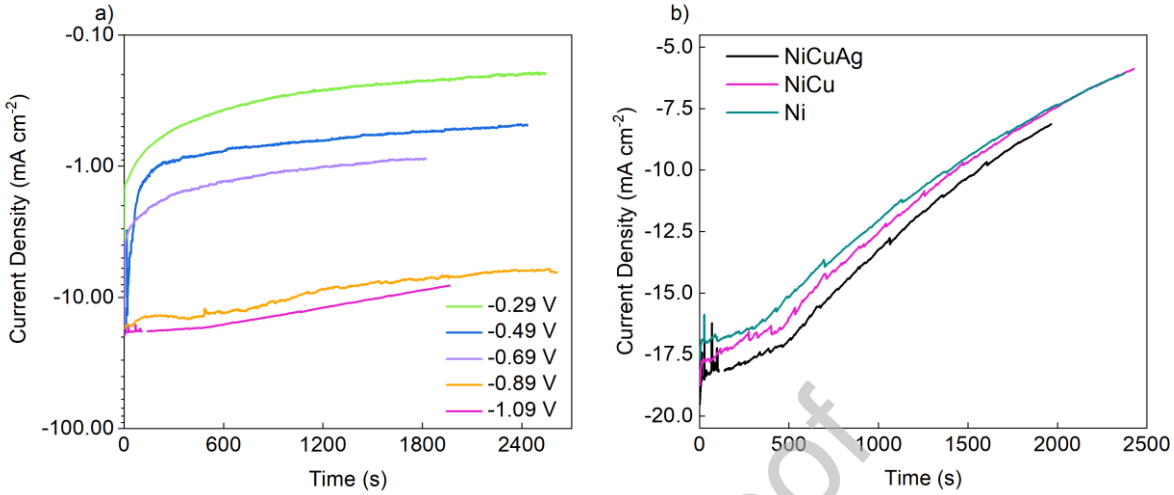

Figure 8. Chronoamperometry of a) NiCuAg at various potentials, and b) a comparison of the performance of NiCuAg with NiCu and Ni at −1.09 V_{RHE}, for the electrochemical reduction of CO_2 in 0.1 M $KHCO_3$ in a custom-made H-cell. Current densities were calculated using the geometric plate area of 2 cm^2.

Faradaic efficiencies (FE) of all products observed are shown in Figure 9. For the 3-layered stack, NiCuAg (Figure 9a), the main products are H_2 and formic acid; the Faradaic efficiency for formic acid ranges from 5% to 16% over the potential range from −0.49 to −1.09 V vs. RHE. At potentials of −0.89 and −1.09 V vs. RHE, methanol is detected at Faradaic efficiencies of 2 ± 0.2% and 1 ± 0.3% respectively. At −1.09 V vs. RHE, ethanol is also seen with a Faradaic efficiency of 2 ± 0.3%. An extended-duration stability test with this electrode was performed at −1.09 V vs. RHE (see Supporting Information, Figure S11), showing that the catalyst maintains significant activity for up to an hour.

Faradaic efficiencies were also measured, at a range of potentials, with the other structures. Figure 9b shows the comparison of the CO_2 reduction products at each stage of the stack synthesis at a potential of −1.09 V vs. RHE. It is clear from this graph that the addition of each layer increased the Faradaic efficiency towards formic acid. The bare Ni plate achieved an FE of 1 ± 0.3%, predominantly

favouring the hydrogen evolution reaction over the reduction of CO_2. The addition of the electrodeposited Cu layer (NiCu) increased the FE for formic acid to 9 ± 1.3%. Meanwhile, the three-layer catalyst, NiCuAg exhibited a Faradaic efficiency of 13 ± 5.1% at the same potential.

Despite this, the highest Faradaic efficiency for formic acid was seen with the two-layer NiCu catalyst, 24 ± 8.5% at −0.89 V vs. RHE. Thus, the addition of the Ag layer may not always be conducive to improved CO_2 reduction. Indeed, Table S5 in the Supporting Information shows that Ni and NiCu in fact give better Faradaic yields for CO_2 reduction to methanol and ethanol than does NiCuAg. On this basis, it seems that there is little evidence to suggest that there is a beneficial synergism for carbon dioxide electroreduction from having Ni, Cu and Ag all in close proximity on the electrode surface.

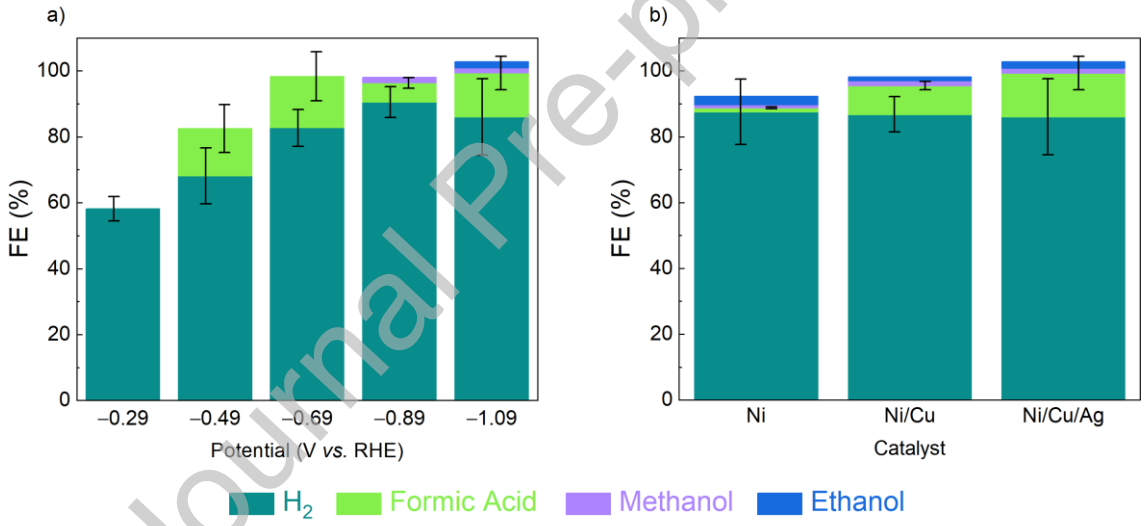

Figure 9. Stacked Faradaic efficiency graphs comparing a) NiCuAg across various potentials, and b) a comparison of the performance of NiCuAg with NiCu and Ni at −1.09 V_{RHE}, for the electrochemical reduction of CO_2 in 0.1 M $KHCO_3$ in a custom-made H-cell.

4. Conclusion

In summary, we have successfully synthesised, characterised, and tested a 3-layer NiCuAg stack as a catalyst for the electrochemical reduction of CO_2. The additional metal layers of copper and silver

were added by electrodeposition and galvanic replacement respectively. The corresponding 2-layer NiCu stack, as well as bare Ni, were also characterised and tested. Analysis of the results of carbon dioxide reduction experiments with these different materials showed that bimetallic NiCu and bare Ni both gave higher Faradaic efficiencies for CO_2 electroreduction to methanol and ethanol than the synthesised trimetallic NiCuAg stacks. There is, therefore, no evidence to support the hypothesis that the combination of Ni, Cu and Ag is conducive to deeper reduction of CO_2 than can be achieved by NiCu or Ni alone. This work has ramifications for the development of multi-metallic catalysts for a range of electrochemical processes, showing that the combination of three individually promising materials does not necessarily lead to improved performance in the resulting ensemble.

Data availability

The data underpinning this study have been deposited in the University of Glasgow's Enlighten database under accession code http://dx.doi.org/10.5525/gla.researchdata.XXXX.

CRediT authorship contribution statement

Hannah Dickinson: Methodology, Data curation, Investigation, Writing – Original Draft Preparation

Mark D. Symes: Conceptualization, Supervision, Writing – review & editing

Declaration of Competing Interest

The authors declare no conflicts of interest.

Acknowledgments

We thank the Geoanalytical Electron Microscopy and Spectroscopy (GEMS) facility in the School of Geographical and Earth Sciences, University of Glasgow for scanning electron microscopy. We thank the Kelvin Nanocharacterisation Centre (KNC) in the School of Physics and Astronomy, University of

Glasgow for cross-sectional transmission electron microscopy and associated techniques. This work was supported by the EPSRC (EP/W033135/1). MDS thanks the Royal Society for a University Research Fellowship (URF\R\211007).

References

1 Intergovernmental Panel on Climate Change, *Climate Change 2021 – The Physical Science Basis*, Cambridge University Press, 2023.

2 L. Li, J. Lin, N. Wu, S. Xie, C. Meng, Y. Zheng, X. Wang and Y. Zhao, *Energy and Built Environment*, 2022, **3**, 139–157.

3 S. Sen and S. Ganguly, *Renewable and Sustainable Energy Reviews*, 2017, **69**, 1170–1181.

4 N. S. Lewis and D. G. Nocera, *Proceedings of the National Academy of Sciences*, 2006, **103**, 15729–15735.

5 K. Malik, S. Singh, S. Basu and A. Verma, *WIREs Energy and Environment*, , DOI:10.1002/wene.244.

6 G. A. Olah, A. Goeppert and G. K. S. Prakash, *J Org Chem*, 2009, **74**, 487–498.

7 M. Gattrell, N. Gupta and A. Co, *Energy Convers Manag*, 2007, **48**, 1255–1265.

8 P. De Luna, C. Hahn, D. Higgins, S. A. Jaffer, T. F. Jaramillo and E. H. Sargent, *Science (1979)*, 2019, **364**, eaav3506.

9 M. Jouny, W. Luc and F. Jiao, *Ind Eng Chem Res*, 2018, **57**, 2165–2177.

10 K. P. Kuhl, E. R. Cave, D. N. Abram and T. F. Jaramillo, *Energy Environ Sci*, 2012, **5**, 7050–7059.

11 D. T. Whipple and P. J. A. Kenis, *J Phys Chem Lett*, 2010, **1**, 3451–3458.

12 A. Bagger, *Curr Opin Electrochem*, 2023, **40**, 101339.

13 Y. Hori, A. Murata and R. Takahashi, *Journal of the Chemical Society, Faraday Transactions 1: Physical Chemistry in Condensed Phases*, 1989, **85**, 2309.

14 R. Kortlever, J. Shen, K. J. P. Schouten, F. Calle-Vallejo and M. T. M. Koper, *J Phys Chem Lett*, 2015, **6**, 4073–4082.

15 A. H. Shah, Y. Wang, A. R. Woldu, L. Lin, M. Iqbal, D. Cahen and T. He, *Journal of Physical Chemistry C*, 2018, **122**, 18528–18536.

16 A. A. Peterson and J. K. Nørskov, *J Phys Chem Lett*, 2012, **3**, 251–258.

17 Y. Li and Q. Sun, *Adv Energy Mater*, 2016, **6**, 1600463.

18 J. He, N. J. J. Johnson, A. Huang and C. P. Berlinguette, *ChemSusChem*, 2018, **11**, 48–57.

19 H. L. A. Dickinson and M. D. Symes, *Electrochem commun*, 2022, **135**, 107212.

20 S. Nitopi, E. Bertheussen, S. B. Scott, X. Liu, A. K. Engstfeld, S. Horch, B. Seger, I. E. L. Stephens, K. Chan, C. Hahn, J. K. Nørskov, T. F. Jaramillo and I. Chorkendorff, *Chem Rev*, 2019, **119**, 7610–7672.

21 J. Zhao, S. Xue, J. Barber, Y. Zhou, J. Meng and X. Ke, *J Mater Chem A Mater*, 2020, **8**, 4700–4734.

22 D. Karapinar, C. E. Creissen, J. G. Rivera de la Cruz, M. W. Schreiber and M. Fontecave, *ACS Energy Lett*, 2021, **6**, 694–706.

23 M. K. Birhanu, M.-C. Tsai, A. W. Kahsay, C.-T. Chen, T. S. Zeleke, K. B. Ibrahim, C.-J. Huang, W.-N. Su and B.-J. Hwang, *Adv Mater Interfaces*, 2018, **5**, 1800919.

24 C. Xiao and J. Zhang, *ACS Nano*, 2021, **15**, 7975–8000.

25 B. Sun, M. Dai, S. Cai, H. Cheng, K. Song, Y. Yu and H. Hu, *Fuel*, 2023, **332**, 126114.

26 J. Hu, F. Yang, J. Qu, Y. Cai, X. Yang and C. M. Li, *Journal of Energy Chemistry*, 2023, **87**, 162–191.

27 M. Watanabe, M. Shibata, A. Kato, M. Azuma and T. Sakata, *J Electrochem Soc*, 1991, **138**, 3382–3389.

28 A. Vasileff, C. Xu, Y. Jiao, Y. Zheng and S.-Z. Qiao, *Chem*, 2018, **4**, 1809–1831.

29 J. Christophe, Th. Doneux and C. Buess-Herman, *Electrocatalysis*, 2012, **3**, 139–146.

30 D. Kim, J. Resasco, Y. Yu, A. M. Asiri and P. Yang, *Nat Commun*, 2014, **5**, 4948.

31 Z. Cai, Y. Wu, Z. Wu, L. Yin, Z. Weng, Y. Zhong, W. Xu, X. Sun and H. Wang, *ACS Energy Lett*, 2018, **3**, 2816–2822.

32 S. Back, J.-H. Kim, Y.-T. Kim and Y. Jung, *ACS Appl Mater Interfaces*, 2016, **8**, 23022–23027.

33 C. G. Morales-Guio, E. R. Cave, S. A. Nitopi, J. T. Feaster, L. Wang, K. P. Kuhl, A. Jackson, N. C. Johnson, D. N. Abram, T. Hatsukade, C. Hahn and T. F. Jaramillo, *Nat Catal*, 2018, **1**, 764–771.

34 Y. Zhu, Z. Gao, Z. Zhang, T. Lin, Q. Zhang, H. Liu, L. Gu and W. Hu, *Nano Res*, 2022, **15**, 7861–7867.

35 J. Gao, H. Zhang, X. Guo, J. Luo, S. M. Zakeeruddin, D. Ren and M. Grätzel, *J Am Chem Soc*, 2019, **141**, 18704–18714.

36 W. Chaitree, A. Hongmeuan, P. Pinthong and J. Panpranot, *Catalysts*, 2023, **13**, 1020.

37 Z.-Y. Zhang, H. Tian, L. Bian, S.-Z. Liu, Y. Liu and Z.-L. Wang, *Journal of Energy Chemistry*, 2023, **83**, 90–97.

38 X. Zhang, C. Liu, Y. Zhao, L. Li, Y. Chen, F. Raziq, L. Qiao, S.-X. Guo, C. Wang, G. G. Wallace, A. M. Bond and J. Zhang, *Appl Catal B*, 2021, **291**, 120030.

39 T. M. Suzuki, T. Ishizaki, S. Kosaka, N. Takahashi, N. Isomura, J. Seki, Y. Matsuoka, K. Oh-ishi, A. Oshima, K. Kitazumi, K. Sekizawa and T. Morikawa, *Chemical Communications*, 2020, **56**, 15008–15011.

40 C. Choi, J. Cai, C. Lee, H. M. Lee, M. Xu and Y. Huang, *Nano Res*, , DOI:10.1007/s12274-021-3639-x.

41 Y. Hori, K. Kikuchi and S. Suzuki, *Chem Lett*, 1985, **14**, 1695–1698.

42 A. Bagger, W. Ju, A. S. Varela, P. Strasser and J. Rossmeisl, *ChemPhysChem*, 2017, **18**, 3266–3273.

43 A. Krishnan, A. Ajith, A. V Krishnan, R. E. Saji, S. Syamli and S. M. A. Shibli, *Surfaces and Interfaces*, 2023, **36**, 102619.

44 V. Vij, S. Sultan, A. M. Harzandi, A. Meena, J. N. Tiwari, W.-G. Lee, T. Yoon and K. S. Kim, *ACS Catal*, 2017, **7**, 7196–7225.

45 X.-H. Liu, X.-L. Jia, Y.-L. Zhao, R.-X. Zheng, Q.-L. Meng, C.-P. Liu, W. Xing and M.-L. Xiao, *Advanced Sensor and Energy Materials*, 2023, **2**, 100073.

46 A. R. Paris and A. B. Bocarsly, *ACS Catal*, 2017, **7**, 6815–6820.

47 A. I. Tsiotsias, N. D. Charisiou, I. V. Yentekakis and M. A. Goula, *Nanomaterials*, 2020, **11**, 28.

48 N. Hoshi, M. Kato and Y. Hori, *Journal of Electroanalytical Chemistry*, 1997, **440**, 283–286.

49 S. Verma, X. Lu, S. Ma, R. I. Masel and P. J. A. Kenis, *Physical Chemistry Chemical Physics*, 2016, **18**, 7075–7084.

50 X.-G. Zhang, X. Jin, D.-Y. Wu and Z.-Q. Tian, *The Journal of Physical Chemistry C*, 2018, **122**, 25447–25455.

51 J. Rosen, G. S. Hutchings, Q. Lu, S. Rivera, Y. Zhou, D. G. Vlachos and F. Jiao, *ACS Catal*, 2015, **5**, 4293–4299.

52 A. V. Naumkin, A. Kraut-Vass, S. W. Gaarenstroom and C. J. Powell, NIST X-ray Photoelectron Spectroscopy Database, http://dx.doi.org/10.18434/T4T88K, (accessed 27 November 2023).

53 C. D. Wagner, W. M. Riggs, L. E. Davis and J. F. Moulder, *Handbook of X-ray Photoelectron Spectroscopy*, Perkin-Elmer Corporation, Eden Prairie, Minnesota, 1979.

54 D. Hwan Kim, D. Hwa Kwak, H. Jun Tak, Y. Jung, K. Jung, S.-H. Park and J. Soo Ko, *Appl Surf Sci*, 2022, **590**, 153083.

55 J.-J. Velasco-Vélez, K. Skorupska, E. Frei, Y.-C. Huang, C.-L. Dong, B.-J. Su, C.-J. Hsu, H.-Y. Chou, J.-M. Chen, P. Strasser, R. Schlögl, A. Knop-Gericke and C.-H. Chuang, *J Phys Chem B*, 2018, **122**, 780–787.

56 V. D. Patake, S. S. Joshi, C. D. Lokhande and O.-S. Joo, *Mater Chem Phys*, 2009, **114**, 6–9.

57 N. Cheng, Y. Xue, Q. Liu, J. Tian, L. Zhang, A. M. Asiri and X. Sun, *Electrochim Acta*, 2015, **163**, 102–106.

58 J. Wang, L. Zhu, L. Ji and Z. Chen, *J Mater Res*, 2018, **33**, 581–589.

59 H. S. Vanegas Parra, S. Calderón Velasco, J. E. Alfonso Orjuela, J. J. Olaya Florez and S. Carvalho, *Coatings*, 2023, **13**, 1154.

60 A. M. Venezia, R. Bertoncello and G. Deganello, *Surface and Interface Analysis*, 1995, **23**, 239–247.

61 K. S. Kim and N. Winograd, *Surf Sci*, 1974, **43**, 625–643.

62 C. L. Bianchi, M. G. Cattania and P. Villa, *Appl Surf Sci*, 1993, **70–71**, 211–216.

63 B. R. Strohmeier, D. E. Levden, R. S. Field and D. M. Hercules, *J Catal*, 1985, **94**, 514–530.

64 T. Nakamura, H. Tomizuka, M. Takahashil and T. Hoshi, *Hyomen Kagaku*, 1995, **16**, 515–520.

65 N. S. McIntyre, S. Sunder, D. W. Shoesmith and F. W. Stanchell, *Journal of Vacuum Science and Technology*, 1981, **18**, 714–721.

66 M. P. Seah, I. S. Gilmore and G. Beamson, *Surface and Interface Analysis*, 1998, **26**, 642–649.

67 G. Johansson, J. Hedman, A. Berndtsson, M. Klasson and R. Nilsson, *J Electron Spectros Relat Phenomena*, 1973, **2**, 295–317.

68 Y. Hori, A. Murata, R. Takahashi and S. Suzuki, *J Chem Soc Chem Commun*, 1988, 17.

69 A. Wuttig, C. Liu, Q. Peng, M. Yaguchi, C. H. Hendon, K. Motobayashi, S. Ye, M. Osawa and Y. Surendranath, *ACS Cent Sci*, 2016, **2**, 522–528.

Declaration of interests

☒ The authors declare that they have no known competing financial interests or personal relationships that could have appeared to influence the work reported in this paper.

☐ The authors declare the following financial interests/personal relationships which may be considered as potential competing interests: